JOURNAL OF SOLID STATE CHEMISTRY 23, 297–314 (1978)

The ac Electrical Behavior of Polycrystalline ZrO_2–CaO

S. H. CHU AND M. A. SEITZ

Metallurgy and Materials Science, College of Engineering, Marquette University, Milwaukee, Wisconsin 53233

Received August 11, 1976; in revised form June 20, 1977

The ac electrical behavior of zirconium oxide with calcium concentrations ranging from 12 to 19 mole% were investigated as a function of frequency, from 100 Hz to 500 kHz, temperature, from 300°C to 900°C, and partial pressure of oxygen, from 10^{-5} to 1 atm. Specimens with different grain sizes, electrode materials, and degrees of sintering were also investigated. The ac electrical behavior of the specimens were analyzed with the aid of impedance plotting techniques ($1/\omega C_s$ vs R_s) and equivalent circuit representation. At high temperatures ($T \gtrsim 650$°C), space charge polarization at the electrodes seemed to be responsible for the observed ac electrical behavior, while at intermediate temperatures ($450 \gtrsim T \gtrsim 650$°C) the grain boundaries contribute an important resistance and capacitance to the specimen equivalent circuit. At low temperatures ($T \lesssim 450$°C), the electrical behavior appears to be influenced by a parallel conduction path, which could be attributed to the high-frequency-limiting capacitance of the bulk material.

Introduction

In recent years, solid electrolytes based on pure or doped oxides (ZrO_2, CeO_2, β-Al_2O_3, etc.) and halides (AgI, AgBr, $RbAg_4I_5$, etc.) have received considerable attention both in basic and applied areas of technology. They have been used in the construction of galvanic cells for measuring thermodynamic and kinetic properties of selected reactions, in the development of oxygen sensors for both gas mixtures and liquid metals, and in the development of solid-state batteries and fuel cells. The suitability of an electrolyte material is determined, to a great extent, by its ionic conductivity and ionic transport number. Previous studies of the transport phenomena within a solid electrolyte have been concentrated in the characterization, at elevated temperatures, of types and concentrations of ionic and electronic defects, and their mobilities as a function of temperature, partial pressure, and dopant concentration. In those studies, sintered polycrystalline specimens were mostly used and certain types of electrodes were applied to the specimen surfaces. Although the electrical transport at the specimen–electrode interface has been investigated by several investigators, little consideration has been given to the influence of grain boundary regions on carrier transport within a solid electrolyte. For well-sintered specimens at high temperatures, the assumption that grain boundaries have a negligible influence is reasonable. However, at intermediate and low temperatures, where extrinsic and microstructural factors become important, the influence of grain boundaries on the total electrical conduction can be considerable. The scatter of experimental results at intermediate and low temperatures as found in the literature, to a great extent, might be attributed to grain boundary phenomena, since the structure and properties of these grain boundary regions are sensitive to specimen fabrication parameters.

The purpose of this investigation is to characterize the influence of grain boundaries on the electrical behavior of polycrystalline

0022-4596/78/2334-0297 $02.00/0

ZrO_2–CaO. ZrO_2–CaO was chosen because (1) it is a simple solid electrolyte system and has extensive application, (2) except for grain boundary phenomena, its physical properties are well understood and available, and (3) the understanding of grain boundary behavior in this electrolyte system will provide valuable information for later analysis of more complicated solid electrolytes. X-ray diffraction (*1*, *2*) studies indicate that ZrO_2 has a cubic fluorite crystal structure within the solubility limit of CaO (10 to 20 mole%). The calcium impurity substitutes for zirconium atoms in the structure leading to the formation of oxygen ion vacancies. Previous conductivity, diffusion, and electrochemical cell measurements (*3–11*) have shown that ionic conductivity due to ionized oxygen vacancies predominates over extended ranges of temperature and oxygen partial pressure. The ionic conductivity decreases and the energy of vacancy motion increases (1.2 to 1.3 eV) with CaO concentration. A conductivity maximum near 14% mole% CaO has also been reported (*10*). The direct current–voltage characteristics of ZrO_2–CaO with various types of electrodes has been investigated by Kröger and coworkers (*12*, *13*). Studies of Tien (*14*) on $Zr_{0.84}Ca_{0.16}O_{1.84}$ and Bauerle (*15*) on $Zr_{0.90}Y_{0.20}O_{2.10}$ also point to the influence of grain boundaries on the electrical conduction in solid oxide electrolytes.

In this study, ac electrical measurements and impedance plotting techniques are used to construct an equivalent circuit representation for the specimens. Measurements were performed on CaO-doped ZrO_2 over the frequency interval 100 Hz to 500 kHz, temperature interval 300 to 900°C, and partial pressure of oxygen from 10^{-5} to 1 atm. Specimens having various calcium concentrations, grain sizes, electrode materials, and degrees of sintering were also investigated. The equivalent circuit approach (*16*) allows one to separate and characterize contributions to the total conductivity from individual types of charge carriers, conduction and polarization mechanisms, and physical regions within the specimen.

Experimental Procedure

Polycrystalline specimens of ZrO_2 doped with CaO (12 to 19 mole% CaO) were prepared by dry mixing the appropriate proportions of ZrO_2 (Wah Chang Albany Corp., purity > 99.9%) and $CaCO_3$ (Fisher Scientific Co., purity > 99.98%). for each composition two types of specimens were prepared, and efforts were made to minimize as much as possible the distribution of grain sizes within the specimens. Specimens with fine grain sizes were prepared from powders which were ball-milled to less than 1 μm average grain size. Specimens with coarse grain sizes were prepared from powders which were collected from 270 to 325 mesh sieves (45 to 55 μm). The powdered mixtures were calcined in air at 1000°C for at least 12 hr, ground slightly in an alumina mortar and pestle, and then pressed (10 000 to 35 000 psi) into disks of $\sim\frac{3}{4}$ in. diameter and $\sim\frac{1}{5}$ in. thickness. The pressed disks were then covered with ZrO_2–CaO powders of the same composition and placed in a calcia-stabilized zirconia crucible. The specimens were then sintered in air in a gas-fired furnace at 2000°C for 7 hr, or at 2000°C, 1700°C, or 1550°C for 3 hrs. All lines on X-ray powder diffraction patterns of specimens thus prepared could be assigned to the cubic fluorite crystal structure. Bulk densities of the after-sintered specimens were determined by measuring volume and mass of the specimens. Percentage theoretical densities were obtained by comparing the bulk densities with theoretical densities based on an oxygen vacancy model. Electrical contact to the specimens was made on their plane parallel surfaces, using either Engelhard No. 601-FM gold paste or Engelhard No. 6082 platinum paste. Thick and uniform coatings were obtained by repeated applications of gold or platinum paste subsequently followed by firing to drive off the organic binders within the pastes. After electrical measurements were completed, metallographic examinations were performed on specimens with fine grain sizes to determine the final specimen average grain

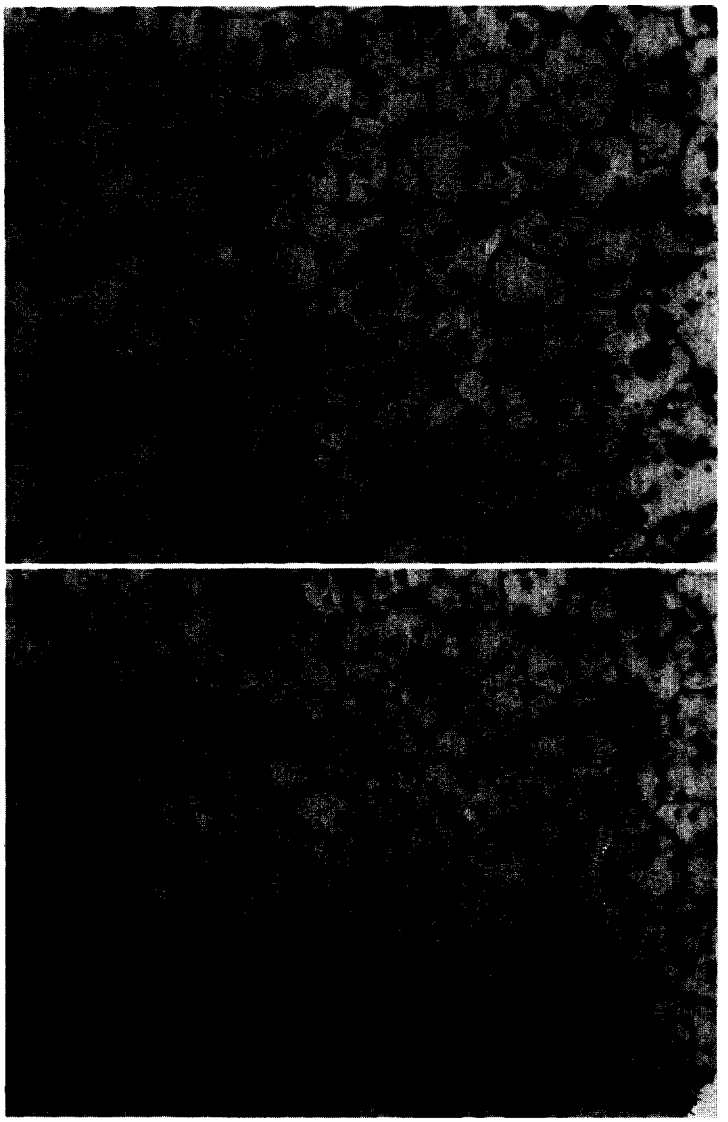

FIG. 1. (a) Micrograph of ZrO_2–CaO (15 mole% CaO, T (sintering) = 1700°C, 342.5×). (b) Micrograph of ZrO_2–CaO (15 mole% CaO, T (sintering) = 1550°C, 342.5×).

sizes after sintering. Representative micrographs are shown in Figs. 1a and 1b. The grain size measurements were made on as-polished and etched surfaces by using the intercept method (Appendix A) (*17*). The coarse grain size specimens, after sintering, did not show significant reduction in physical dimensions and porosities. Micrographs could not be obtained for these porous specimens because of difficulties in polishing and etching. However, no significant change in grain sizes should be expected since sintering and grain growth did not seem to occur significantly in these specimens. SEM and microprobe analysis revealed no impurity segregation at the grain boundaries. In Table I parameters for samples investigated in this work are listed.

The measurement technique and apparatus, as described elsewhere (*16*), is based on the substitution method as developed by Seitz *et*

TABLE I
PARAMETERS FOR SAMPLES INVESTIGATED

Sample	CaO added (mole%)	Initial grain size (μm)	Sintering	Final grain size (μm)	L/A[a]	Theoretical density (%)	Electrodes
1	12	<1	1700°C, 3hr	30	0.3052	87.73	Gold
2	13.5	<1	1700°C, 3hr	30	0.2656	88.24	Gold
3	15	<1	1700°C, 3hr	35	0.2620	88.65	Gold
4	19	<1	1700°C, 3hr	34	0.2421	90.95	Gold
5	15	<1	1550°C, 3hr	22	0.2331	86.07	Gold
6	12	45–55	1700°C, 3hr	45–55	0.2637	67.85	Gold
7	15	45–55	1700°C, 3hr	45–55	0.2234	69.96	Gold
8	17	45–55	1700°C, 3hr	45–55	0.2773	61.25	Gold
9	19	45–55	1700°C, 3hr	45–55	0.2093	68.16	Gold
10	15	45–55	1550°C, 3hr	45–55	0.2081	56.42	Gold
11	15	Random	2000°C, 7hr	30	0.2988	79.00	Gold
12	15	Random	2000°C, 3hr	—	0.2266	63.05	Platinum

[a] L = sample thickness; A = electrode area.

al. (*18*). With this technique the capacitance of specimens having a total resistance of greater than 100 ohms and a dissipation factor less than 10^4 can be measured within ±15%. For mid-range frequencies (1 to 50 kHz) the error is less than ±5%.

The specimens were loaded into a specimen holder and into the measurement system. For each temperature and P_{O_2} provided experimentally, the specimen capacitance and resistance were measured at selected frequencies from 100 Hz to 500 kHz. The specimen temperature was then decreased at 50°C intervals and the P_{O_2} was also reduced. After equilibration was achieved, the above measurement procedure was repeated. Temperatures from room to 900°C were obtained with a kanthal-wound resistance furnace regulated to ±1°C. Values of P_{O_2} were obtained by means of Ar–O_2 gas mixtures.

Experimental Results

(i) *General*

The equivalent parallel capacitance, C_p, and resistance, R_p, of polycrystalline ZrO_2–CaO specimens were measured as a function of frequency, f, in the range of 100 Hz to 500 kHz, over the temperature interval 300 to 900°C, and oxygen partial pressure interval 10^{-5} to 1 atm. Representative isothermal plots of C_p versus frequency, f, are shown in Figs. 2a and 2b. On these figures, three regions of differing behavior can be defined. In region A, the capacitance, C_p, varied as

$$C_p \propto 1/(1 + (\omega\tau)^n), \qquad (1)$$

where ω is the frequency in radians, τ is a relaxation time, and n is a constant between 0.7 and 2.0. In region C, the capacitance varied as

$$C_p \propto \omega^{-m}, \qquad (2)$$

where m is a constant having values between 1 and 1.5. In region B, the capacitance did not vary significantly with the frequency. The equivalent parallel resistances, R_p, were found to decrease with frequency. However, the dispersions were not very pronounced.

(ii) *Impedance Analysis*

In order to elucidate the phenomena responsible for the differing behavior obtained in regions A, B, and C the data were analyzed using impedance-plotting techniques. The total

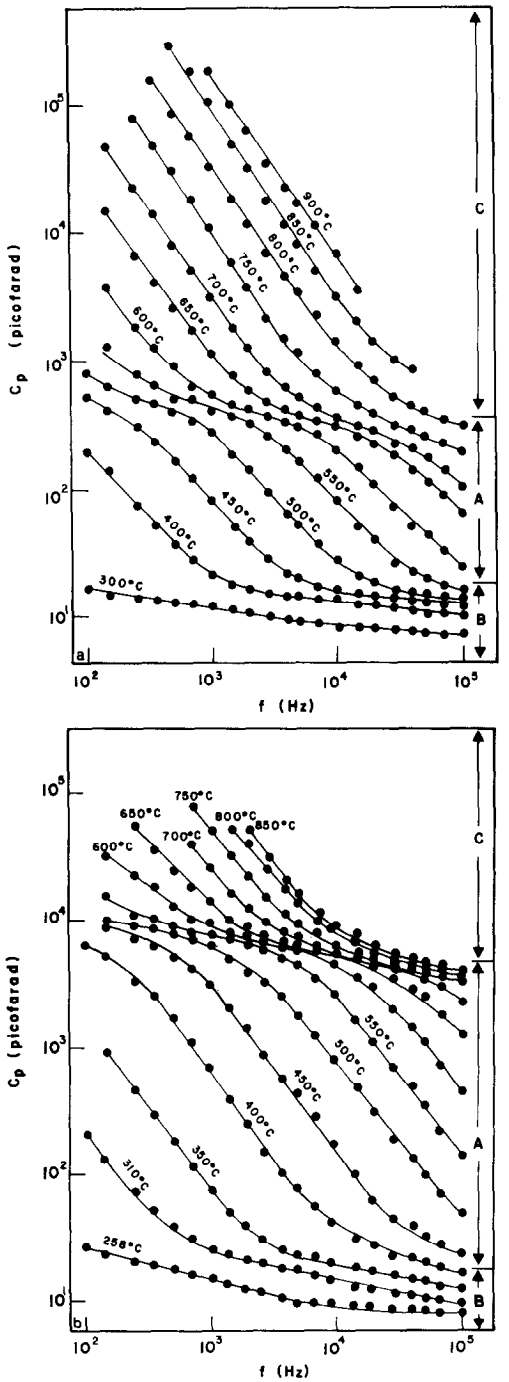

FIG. 2. (a) Capacitance vs frequency for ZrO_2–CaO (15 mole% CaO, random grain size, T (sintering) = 2000°C, gold electrodes, P_{O_2} = 1 atm). (b) Capacitance vs frequency for ZrO_2–CaO (12 mole% CaO, 30 μm average grain size, T (sintering) = 1700°C, gold electrodes, P_{O_2} = 1 atm).

impedance of the specimens were obtained from C_p and R_p as

$$Z = R_s - j(1/\omega C_s) \quad (3)$$

$$= (1/R_p + j\omega C_p)^{-1}. \quad (4)$$

The negative of the imaginary part of the impedance, $1/\omega C_s$, was then plotted against the real part, R_s. In Figs. 3a to 3e the impedance plots for several specimens at various measurement temperatures are shown. These plots typically contain several loops, which suggest a total equivalent circuit representation of the specimen as depicted in Fig. 4. As will be discussed later, the equivalent circuit associated with loop A consists of resistance R_1 representing bulk grains and resistance R_2, as well as capacitance C_2, representing influence of grain boundaries. Loop C is associated with the electrode–specimen interface and is represented by the resistance R_5 and capacitance C_5. Loop B appears to represent a parallel conduction path, and the equivalent circuit for this loop is represented as C_4.

(iii) *Behavior of Loop A*

In order to elucidate the physical phenomena responsible for the behavior resulting in loop A, the influence of calcium content, sintering, and grain size were investigated. The effects of these variations on the values of R_1 are shown in Fig. 5. As shown in this figure, the resistance R_1 decreased exponentially with temperature. The magnitudes of R_1 and its activation energy increased with calcium concentration (1.13 to 1.29 eV). Variations with grain size and sintering temperatures were also noted. The data showed negligible dependence of R_1 on oxygen partial pressure. The effects of specimen sintering, grain size, and CaO concentration on values of R_2 and C_2 are given in Figs. 6 and 7. As shown in Fig. 6 the resistance R_2 also decreased exponentially with temperature. An increase of R_2 for specimens having higher CaO concentrations, larger grain sizes, and lesser sintering were also observed. A slightly higher activation

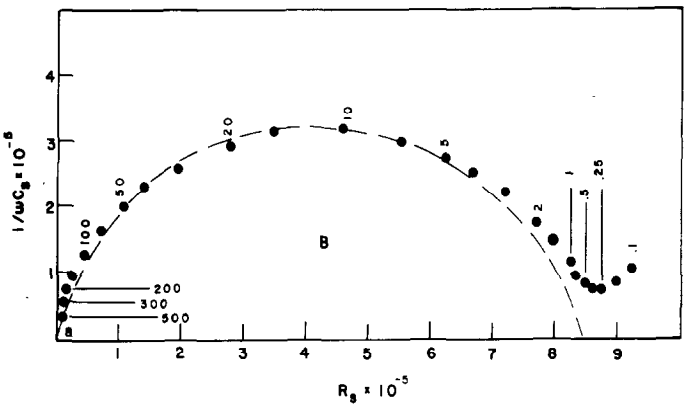
B
200
300
500
a
$R_s \times 10^{-5}$

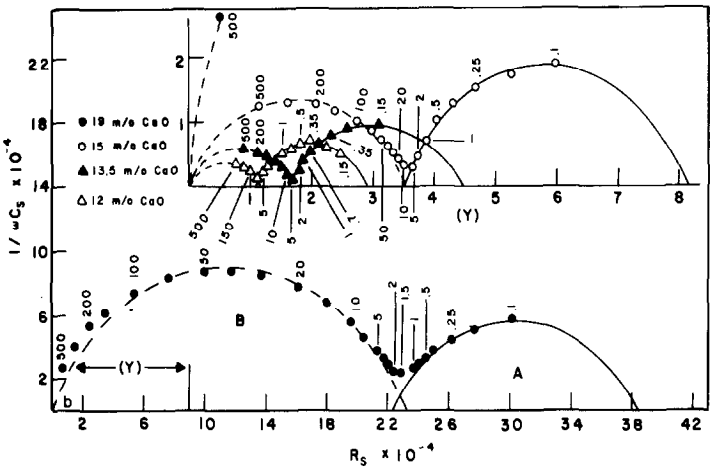
19 m/o CaO
15 m/o CaO
13.5 m/o CaO
12 m/o CaO
(Y)
B
A
b
$R_s \times 10^{-4}$

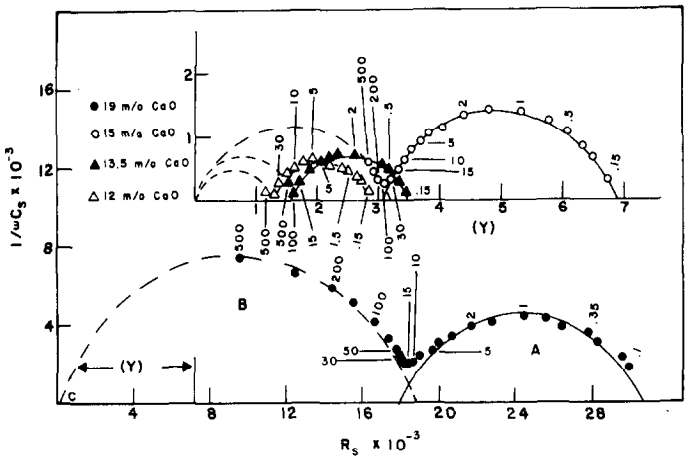
19 m/o CaO
15 m/o CaO
13.5 m/o CaO
12 m/o CaO
(Y)
B
A
c
$R_s \times 10^{-3}$

FIGURE 3

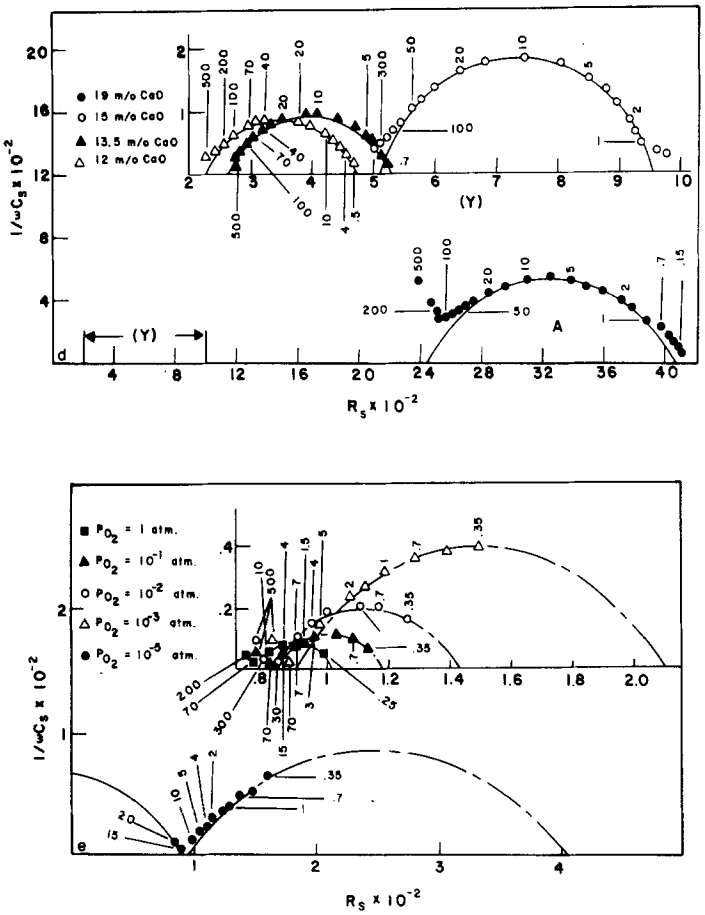

FIG. 3. (a) Impedance of ZrO_2–CaO at 350°C (15 mole% CaO, T (sintering) = 1700°C, gold electrodes, P_{O_2} = 1 atm, frequencies are shown in kHz). (b) Impedance of ZrO_2–CaO at 450°C for four CaO concentrations (T(sintering) = 1700°C, gold electrodes, P_{O_2} = 1 atm, frequencies are shown in kHz). (c) Impedance of ZrO_2–CaO at 550°C for four CaO concentrations (T(sintering) = 1700°C, gold electrodes, P_{O_2} = 1 atm, frequencies are shown in kHz). (d) Impedance of ZrO_2–CaO at 650°C for four CaO concentrations (T(sintering) = 1700°C, gold electrodes, P_{O_2} = 1 atm, frequencies are shown in kHz). (e) Impedance of ZrO_2–CaO at 850°C as a function of P_{O_2} (15 mole% CaO, T(sintering) = 2000°C, platinum electrodes, frequencies are shown in kHz).

energy (1.23 to 1.49 eV) was noted for R_2 as compared to R_1 for all the specimens investigated. Values of R_2 were also found to be comparable to R_1 and exhibited no significant partial pressure dependence. The capacitance C_2, as shown in Fig. 7, was found to be relatively independent of composition, temperature, and oxygen partial pressure. Those capacitance values were generally larger for specimens having smaller grain sizes and for specimens sintered at higher temperatures.

(iv) *Behavior of Loop B*

Loop B was observed at low temperatures ($T \lesssim 450$°C) and high measurement frequencies. Qualitatively, it was noticed that the influence of loop B was evident at comparatively higher temperatures for specimens with larger grain sizes, lower degrees of sintering, and higher CaO contents. Loop B appears to pass through the origin on the impedance plots. The capacitances associated with this

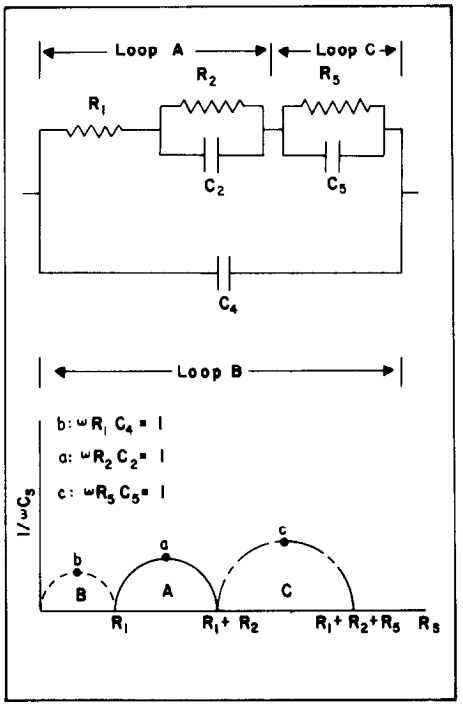

FIG. 4. Equivalent circuit representation and impedance plot of ZrO_2–CaO.

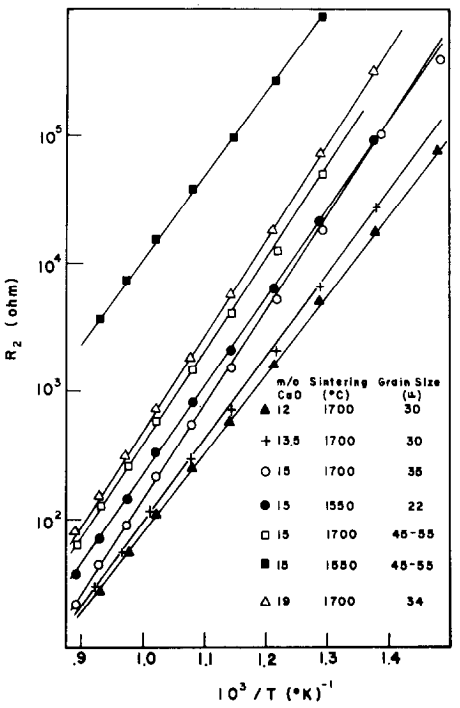

FIG. 6. Boundary resistance, R_2, vs temperature for ZrO_2–CaO (gold electrodes, $P_{O_2} = 1$ atm).

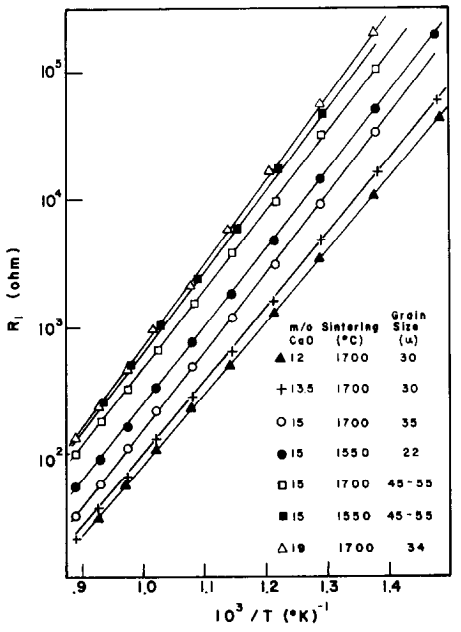

FIG. 5. Bulk resistance, R_1, vs temperature for ZrO_2–CaO (gold electrodes, $P_{O_2} = 1$ atm).

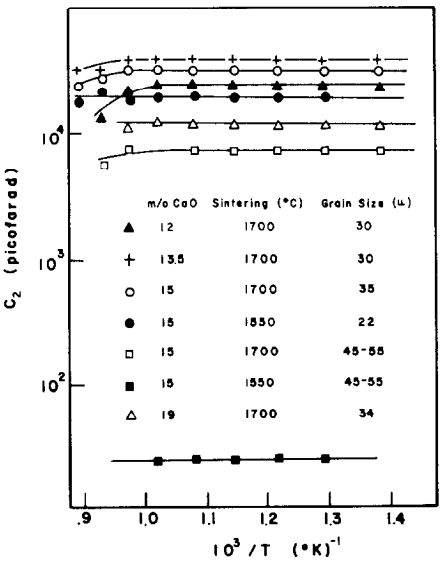

FIG. 7. Boundary capacitance, C_2, vs temperature for ZrO_2–CaO (gold electrodes, $P_{O_2} = 1$ atm).

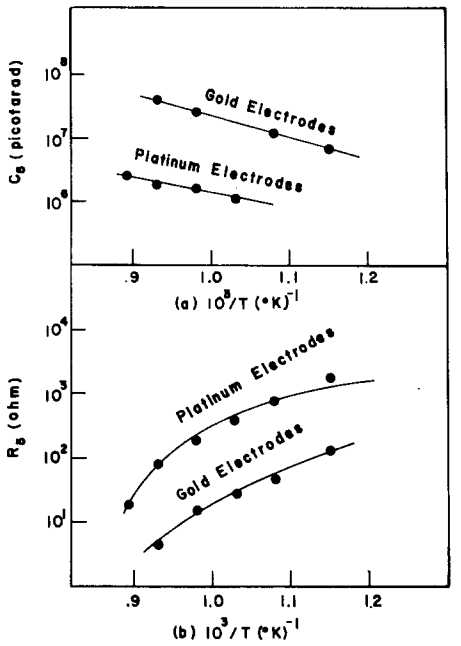

FIG. 8. (a) Electrode capacitance, C_5, (b) electrode resistance, R_5, vs temperature for ZrO–CaO (15 mole% CaO, T(sintering) = 2000°C, P_{O_2} = 1 atm).

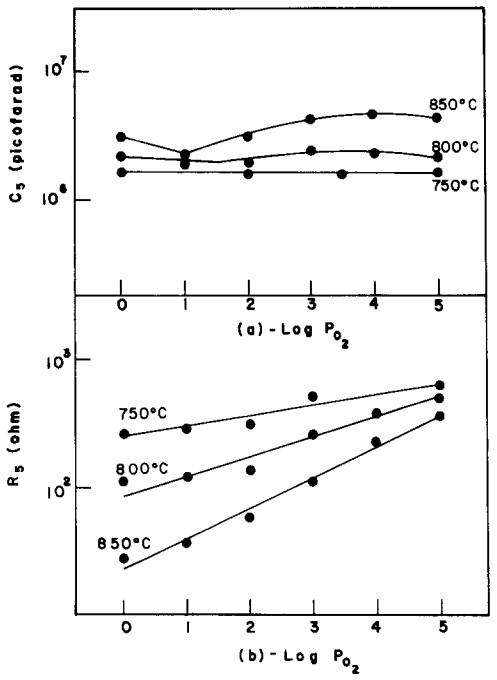

FIG. 9. (a) Electrode capacitance, C_5, (b) electrode resistance, R_5, vs P_{O_2} for ZrO_2–CaO (15 mole% CaO, T(sintering) = 2000°C, platinum electrodes).

loop were on the order of 10 pF, and exhibited negligible dependence on the various experimental variables.

(v) *Behavior of Loop C*

Loop C, as shown in Figs. 3a to 3e, was observed at high temperatures ($T \gtrsim 650$°C). This loop corresponds to region C in Fig. 2, where the total capacitance, C_p, decreased as ω^{-m}. Its influence was more significant for specimens sintered at 2000°C and was found to be dependent on temperature, electrode material, and partial pressure of oxygen. The contribution of loop C to the total equivalent circuit is represented by equivalent circuit parameters R_5 and C_5. Plots of R_5 and C_5 as a function of temperature and P_{O_2} are given in Figs. 8 and 9. The data trends indicated that values of C_5 were much larger than C_2. With increasing temperature the capacitance C_5 increased while the resistance R_5 decreased. Both C_5 and R_5 were found to increase at reduced partial pressures. Variations of R_5 and C_5 with electrode materials were also noted.

Discussion

(i) *Loop A*

The bulk conductivity, σ_1, was obtained from the resistance R_1 by correcting for specimen geometry and porosity. These values are compared with the results of previous studies in Fig. 10. It should be noted that in these previous studies, the total electrical conductivity of polycrystalline specimens at certain frequencies (1 kHz in most cases) were considered, while in this study σ_1, as obtained from impedance analysis, represent dc bulk conductivity of the specimen. It is seen in Fig. 10 that σ_1 agrees well with extrapolations of previous conductivity values to lower temperatures. The agreement suggests that grain boundaries have little contribution to the electrical behavior at elevated temperatures. Compositional dependences of σ_1 were also found to agree with previous findings.

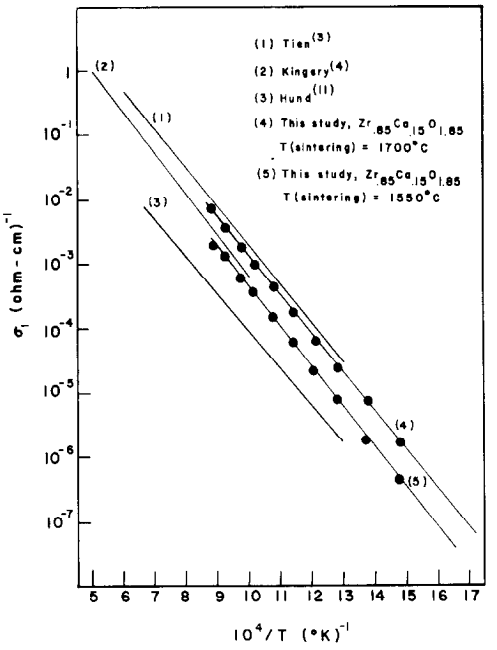

FIG. 10. Bulk conductivity, σ_1, vs temperature for ZrO_2–CaO (15 mole% CaO).

The influence of grain size and specimen sintering was found to become increasingly important as the measurement temperature was decreased. This influence is manifested in the values of R_2 and C_2 as are shown in Figs. 6 and 7. In the case of samples 3 and 5, which had CaO concentrations of 15 mole% and final grain sizes of 35 and 22 μm, a simple model can be used to elucidate this interrelationship. The relative values of R_2 and C_2 for these specimens can be rationalized on the basis of a model consisting of a cubical array of cubical grains, where it is assumed that the individual grain boundary thickness and resistivities are the same for all boundaries. The values of R_2 and C_2 should then differ by a factor related to the ratio of their grain sizes, which in turn is related to the number of boundaries between the electrodes of the specimen. This simplified model appeared to be adequate in the case where significant recrystallization and grain growth had occurred. However, where little grain growth was observed or where there were compositional variations, a more complicated model was warranted.

The authors have elected to choose a model consisting of a cubical array of uniform spherical grains, as is described in Appendix B. This model allows a relatively simple means of representing the equivalent circuit parameters of the boundaries (R_2 and C_2) and bulk (R_1), while considering the influence of both grain size and degree of sintering. In a polycrystalline sample, the geometric packing among individual grains is related to grain geometry, size distribution, and porosity. In the present model, minor variations of grain size, and grain and grain boundary geometry can be accounted for by a suitable packing parameter, α. If there are extreme variations of grain size or if the individual grain boundaries differed significantly one from the other, the impedance plots of Fig. 3 would be nearly flat and it would be impossible to obtain values for the aforementioned equivalent circuit parameters.

The relationships obtained in Eqs. (B1)–(B13) aid in understanding the variations of R_2 and C_2 with varying degrees of sintering and differing grain sizes. The data of the present study were found to agree with the predictions of the chosen model reasonably well. As expected, the capacitance C_2 increases and the resistance R_2 decreases with decreasing grain size. For low degrees of sintering, the intergranular contact area A_2 would show a significant increase for specimens which are sintered at higher temperatures, longer times, and having smaller initial grain sizes. This geometric variation of the boundaries leads to a decrease of the ratio, l_2/A_2. An increase in capacitance C_2 and a decrease in resistance R_2 would be expected if the dielectric constant, ε_2, and resistivity, ρ_2, are not significant functions of sintering. For the same reason, the anomalous increase in resistance R_2 and decrease in capacitance C_2 for sample 10, with 15 mole% CaO sintered at 1550°C and with 45–55 μm grain size, are understandable. Due to coarse initial grain size and low sintering temperatures, sintering has not occurred in this

TABLE II
ESTIMATED GEOMETRIC PARAMETERS (l_2/A_2) FOR FOUR $Zr_{0.85}Ca_{0.15}O_{1.85}$ SPECIMENS[a,b]

Specimen	D (μm)	L/A (cm^{-1})	C_2 (pF)	l_2/A_2 (cm^{-1})	A_2 (cm^2)	l_2 (Å)
3	35	0.2620	3.16×10^4	0.117	8.14×10^{-6}	95
5	22	0.2331	2×10^4	0.327	2.84×10^{-6}	93
7	45–55	0.2234	7.5×10^3	0.369	—	—
10	45–55	0.2081	23.7	133	—	—

[a] Physical meanings of the symbols are defined in Appendix B.
[b] Assume $\varepsilon_2 \sim 30$.

particular sample and in fact it might be considered as a slightly sintered powder compact. The effective contact area A_2 would be very small, which would account for the anomaly.

For all the samples investigated, the activation energy of R_2 was higher than that for R_1. Also, it was found that R_2 was less than R_1 at higher temperatures and the reverse is true at lower temperatures. This observation suggests that the contribution from the grain boundary regions to the total sample resistance is insignificant at high temperatures. However, at low temperatures the sample resistance is dominated by the boundary resistance.

Based on the present physical picture that R_2 and C_2 are associated with the same physical region, the geometric parameter, l_2/A_2, and the materials parameter, ρ_2, of the boundary regions can be estimated by using Eqs. (B10) and (B13) and by choosing a reasonable value for ε_2 (~30 for ZrO_2–CaO). By further applying metallographic analysis (Appendix A) values of the effective intergranular contact area A_2 and the effective boundary thickness l_1 can be estimated. Results of this type of analysis for several specimens are shown in Tables II and III. In further discussion the resistivities of the bulk, ρ_1, and boundaries, ρ_2, are considered. Unlike the resistance, R_1 and R_2, these parameters do not contain geometric factors and, therefore, are more representative of the materials properties of the two regions.

It is seen from Table III that τ_2 varied with specimen grain size and sintering. τ_2 was also found to vary with CaO concentration. These variations would be related to effective resistivity changes in the grain boundary regions. Table III also shows that the effective resistivity of the boundary regions are much higher than the bulk resistivity with the resistivity ratio of boundary to bulk on the order of 10^3. High resistivity boundaries have also been observed in several other materials (*19–22*). There has been no consensus yet concerning the physical interpretation of this behavior. The difficulty arises since the high resistivity can be attributed to either low charge carrier concentration or low charge carrier mobility. In this study, except for a slightly higher activation energy ($\Delta E \sim 0.2$ eV), consistent trends were observed for R_2 and R_1 as functions of temperature, CaO concentration, and P_{O_2}. This tends to suggest that the electrical conduction mechanism within the grain boundaries is similar to that within the bulk material, i.e., ionic conduction via vacancy diffusion. It does not seem unreasonable to account for the higher resistivity of these regions on the basis of a reduced effective charge carrier concentration at the boundaries.

Lehovoc (*23*), Allnatt (*24*), and Kliewer and Koehler (*25*, *26*) have demonstrated that, at thermodynamic equilibrium, static-space-charge regions should exist adjacent to the surfaces of an ionic single crystal due to differences in the Gibbs free energy of formation for various types of defects or due to

surface or contact potential at the crystal surface. For small ac fields the space charge region acts like a barrier layer or high resistivity region. For large ac fields, the field-induced oscillation of a static-space-charge distribution about its equilibrium value lead to an added space charge capacitance. In a polycrystalline specimen, although the thickness of an individual boundary is small, the influence of the boundary space charge layers might be significant due to the fact that a large number of boundaries exist. A number of physical processes beyond those stated by Lehovoc (*23*) might also be responsible for static-space-charge layers at the grain boundaries. First, the calcium dopant, which substitutes for zirconium atoms near the surface, might not form vacancies as readily as would be the case in the bulk structure since vacancies might not be needed to fulfill nearest-neighbor charge compensation requirements. Second, oxygen chemisorption at the grain boundaries could result in a decrease of mobile vacancy concentration. This would be the case if the adsorbed oxygen combined with a vacancy to form a normal oxygen site or combined with zirconium atoms on the surface to form added molecules of ZrO_2. Normally, a P_{O_2} dependence of surface resistivity or capacitance would be a manifestation of chemisorption processes. In this study, negligible oxygen partial pressure dependencies were observed for the values of R_2 and C_2. It seems then that if chemisorption were responsible, the predominant process would have had to occur at higher temperatures and be irreversible at lower temperatures. This latter situation is felt to be quite likely and is to be investigated in future studies. Third, impurity or phase segregation at the grain boundaries might lead to a lower carrier concentration. Direct observations of solute segregation and phase separation within the boundary regions have been found in several ceramic oxides (*27*, *28*). The segregation was thought to take place, most likely, during specimen cooling after high-

TABLE III

ESTIMATED MATERIAL PARAMETERS (ρ_2, ρ_1, and ρ_2/ρ_1) FOR THREE $Zr_{0.85}Ca_{0.15}O_{1.85}$ SPECIMENS[a–d]

	800°C				500°C			
Specimen	τ_2 (sec)	ρ_2 (ohm cm)	ρ_1 (ohm cm)	ρ_1/ρ_1	τ_2 (sec)	ρ_2 (ohm cm)	ρ_1 (ohm cm)	ρ_2/ρ_1
3	1.31×10^{-6}	4.93×10^5	2.1×10^2	$\sim 2 \times 10^3$	6.5×10^3	2.45×10^{-4}	3.8×10^4	$\sim 6.4 \times 10^3$
5	1.43×10^{-6}	5.39×10^5	3.82×10^2	$\sim 1.4 \times 10^3$	4.14×10^{-4}	1.34×10^8	6.8×10^4	$\sim 2.0 \times 10^3$
7	9.22×10^{-7}	3.47×10^5	7.9×10^2	~ 450	3.55×10^{-4}	1.56×10^8	1.42×10^5	$\sim 1.1 \times 10^3$

[a] Physical meanings of symbols are defined in Appendix B.
[b] $\tau_2 = R_2 C_2$.
[c] Assume $\varepsilon_2 \sim 30$.
[d] The bulk resistivity, ρ_1, was calculated from values of R_1 and Eq. (B14).

temperature sintering. SEM studies for several ZrO_2–CaO specimens, however, revealed no nonuniformity in calcium concentration in the vicinity of the boundary regions, nor could a second phase be identified on X-ray diffraction patterns. The data obtained in this study were not sufficient to discriminate among the above processes. The physical origin of the high resistivity in the grain boundaries in this material must, therefore, remain open until further added studies are carried out.

Bauerle (*15*) has investigated the ac electrical behavior of yttria-doped zirconium oxide as a function of temperature and P_{O_2}. The grain boundary contribution to the total specimen admittance was attributed to a constriction resistance across the grain-boundary contact regions, while the capacitance was attributed to blocking of ionic charge carriers by an impurity phase between grain boundaries. In this study, the influence of specimen sintering, grain size, and CaO contents were further investigated. It was found that the present single region model is more adequate in explaining the temperature, P_{O_2}, and compositional dependences of R_2 and C_2. It could also explain the observed decrease in R_2 and increase in C_2 for specimens having higher degrees of sintering and smaller grain sizes. In terms of Bauerle's idealized two-region model, the capacitance C_2 would decrease for well-sintered specimens. This is the case since more sintering increases the intergranular grain contact areas and, therefore, would either minimize the impurity phase contact areas or reduce the amount of charge carriers being blocked at the impurity phases. Investigation of specimens having different impurity levels also did not show a direct relationship with C_2.

In an early study, Lay (*29*) has attributed the dielectric behavior of CaO-doped CeO_2 over the temperature range 0 to 300°C to the relaxation of dipoles resulting from cation–vacancy defect complexes. In this analysis, it has been shown that the concentration of those dipoles is significant only at low temperatures and can be expressed as

$$N = \frac{144\varepsilon_0 kT}{a_0^2 e^2} \cdot \frac{\varepsilon_s - \varepsilon_\infty}{(\varepsilon_s + 2)(\varepsilon_\infty + 2)}. \quad (5)$$

Here, ε_s and ε_∞ are the static and high-frequency-limiting dielectric constants, a_0 is the lattice parameter, ε_0, k, T, and e have their usual meanings. Substituting values obtained from data ($\varepsilon_s \sim 10^3$, $\varepsilon_\infty \sim 30$, $a_0 \sim 5 \times 10^{-8}$ cm) and constants ($\varepsilon_0 = 8.85 \times 10^{-14}$ F/cm, $k = 1.38 \times 10^{-23}$ J/°K, $e = 1.6 \times 10^{-19}$ C) into Eq. (5) yields $N \sim 7 \times 10^{19}/cm^3$ at 800°K. Such a concentration is about 1.5% of the total vacancies available ($\sim 4.4 \times 10^{21}/cm^3$), which is much higher than that predicted by Lay at 800°K. It should be noted that the degree of sample sintering, which does not vary the dipole concentration substantially, has influence on magnitudes of R_2 and C_2 only. Their behavior with temperature is similar. Therefore it is not likely that the observed electrical behavior in this study can be attributed to dipole relaxation of defect complexes.

(ii) *Loop B*

It was found that the low-temperature/high-frequency loop (i.e., loop B) existed at comparatively higher temperatures for specimens with larger grain size, lower degrees of sintering, and higher CaO concentrations. Under these experimental conditions the bulk resistance, R_1, boundary resistance, R_2, and their sum, $R_1 + R_2$, were found to have relatively higher values. Qualitatively, these behaviors indicate that loop B represents a parallel conduction path at low temperatures and high frequencies. As shown in Figs. 3a–3b, within extrapolation error, it appears that loop B would pass through the origin on the impedance plots Therefore, the equivalent circuit associated with loop B can be represented by a capacitance, C_4. Values of C_4 were found to be in the range of 10 to 20 pF and exhibited negligible dependencies on the various experimental variables. Using the physical picture as shown in Fig. B1 and Eq.

(B13), the total capacitance of the bulk grains, C_1, is found to be approximately 10 pF. Therefore, it appears that C_4 can be attributed to the high-frequency-limiting capacitance of the bulk material. The capacitance C_4 used in the present equivalent circuit is analogous to the geometric capacitance, C_g, in Macdonald's equivalent circuit representation of solid electrolytes (*30*).

(iii) *Loop C*

The variations of loop C, observed at high temperatures ($T \gtrsim 650$°C), with P_{O_2} and electrode materials (Figs. 3a to 3e) indicate that the physical phenomena responsible for loop C are related to the specimen–electrode interface. The equivalent circuit associated with loop C has been represented by R_5 and C_5 as shown in Fig. 4. It was found that loop C corresponds to region C in Figs. 2a and 2b. In this region the specimen capacitance exhibited a $\frac{3}{2}$ slope over a wide frequency range. At a fixed measurement frequency the capacitance varied exponentially with temperature. Also, the capacitance did not approach a limiting value at low frequencies. This electrical behavior is in general agreement with previous observations for several ceramic oxides (*31–33*) and have been qualitatively explained in terms of space charge polarization at the electrode–specimen interface. For oxide electrolytes at high temperatures, surface-related polarization due to static or dynamic space charge would be expected because of higher carrier mobilities and fast carrier transport to the electrodes. Several theoretical treatments of static- or dynamic-space-charge polarization have been considered in the literature. In the dynamic situation, three limiting cases were found to be of interest as they lead to large dispersions in the specimen capacitance. These are (a) one mobile species which is partially blocked at the electrodes (*34*), (b) two mobile species, one of which is blocked at the electrodes (*35*), and (c) two mobile species, both of which are blocked at the electrodes (*35*). Results of these analyses have been used to interpret the dielectric behavior of several oxides (*31–33*) and halides (*34–36*).

It is generally accepted that the predominant charge carrier in ZrO_2–CaO, under the experimental conditions investigated in this study, are ionized oxygen vacancies and that the concentrations of electronic charge carriers are negligible. Beaumont and Jacobs (*34*) have considered space charge polarization for the limiting case of a single type of charge carrier being partially blocked at the electrodes. Their results show that the specimen capacitance and resistance would exhibit a Debye-type dispersion. The equivalent circuit as shown in Fig. 11 can adequately describe this behavior. Values of C_5 ($\sim 2 \times 10^6$ to 4×10^7 pF) obtained from loop C were found, however, to be much less than the predicted value of C_{sp} ($\sim 2 \times 10^8$ pF). Also, the temperature dependence of C_5 and C_{sp} were not consistent with each other. These discrepancies might be the result of a too simplified representation of the specimen–electrode interface. As shown in Fig. 11, the specimen–electrode interface is represented by a diffuse double-layer capacitance, C_{sp}, and an electrode resistance, R_{sp}. It is felt that the high degree of porosity in the polycrystalline specimens would allow discharge of vacancies to occur by direct electro-

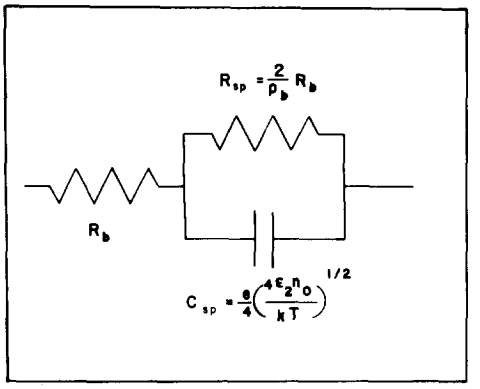

FIG. 11. Equivalent circuit representation of a specimen having space charge polarization (single type of carrier, partial blocking at electrodes).

chemical reaction with the gas phase in the vicinity of the electrode. These reactions are dependent on the carrier concentrations near the electrodes and they can be considered as a faradaic- or Warburg-type process (*37*). The observed increase of R_5 and C_5 at reduced oxygen partial pressures and the increase (decrease) of C_5 (R_5) at higher temperatures seem to suggest that this is the case. The physical structure of the electrode–specimen interface when Warburg-type reactions are considered could be rather complicated. The specimen configurations of this study, however, do not allow further detailed analyses.

Conclusions

The ac electrical behavior of polycrystalline ZrO_2–CaO with calcium concentrations ranging from 12 to 19 mole% were investigated as a function of frequency, from 100 Hz to 500 kHz, temperature, from 300 to 900°C, and partial pressure of oxygen, from $\sim 10^{-5}$ to 1 atm. Specimens with different grain sizes, electrode materials, and degrees of sintering were also investigated. With the aid of impedance plotting techniques, an equivalent circuit representation for the specimens was deduced from the ac electrical data. The electrical components within the equivalent circuit were related to various physical regions within the specimens, and conduction and polarization mechanisms.

At intermediate temperatures ($450 \lesssim T \lesssim 650$°C) the electrical behavior of ZrO_2–CaO can be adequately described by an equivalent circuit composed of a resistance, R_1, representing bulk grains, in series with a parallel network composed of a resistance, R_2, and a capacitance, C_2, representing grain boundaries. The values of the resistance R_1 agreed well with extrapolations of previous conductivity studies to lower temperatures, which suggest that grain boundaries have little influence on the electrical behavior at elevated temperatures ($T \gtrsim 650$°C). Below 650°C the influence of the grain boundary regions becomes increasingly important. The behavior of R_2 and C_2 as functions of temperature, P_{O_2}, CaO concentrations, grain size, and sintering could be rationalized in terms of a model that attributed these qualities to the grain boundary contact regions. The observed increase in C_2 and decrease in R_2 for specimens having smaller grain sizes and higher degrees of sintering was attributed to variations of the geometric parameters of the boundaries (number and thickness to area ratio of the boundaries). The effective resistivity of the boundary regions was estimated from the quantity $\tau_2 = R_2C_2 = \rho_2\varepsilon_2$. It was found that the boundary regions had a much higher resistivity than that of the bulk. The high resistivity of the boundary regions was felt to result from low ionic carrier concentrations in the vicinity of the grain boundary regions.

At high temperatures ($T \gtrsim 650$°C) the electrode-specimen interface presents an important impedance to the total electrical conduction. The equivalent circuit of this region was taken to be a parallel network composed of a resistance, R_5, and capacitance, C_5, which were in series with the aforementioned intermediate temperature circuit. The behavior of R_5 and C_5 as functions of temperature, partial pressure of oxygen, and electrode material could be adequately explained, in a qualitative sense, by assuming space charge polarization due to single type of charge carrier, oxygen vacancies, which are partially blocked at the electrodes. The carrier discharge might involve faradaic- or Warburg-type processes via direct electrochemical reactions of oxygen vacancies with the gas phase.

At low temperatures ($T \lesssim 450$°C), the electrical behavior was influenced by a parallel conduction path. A parallel capacitance, C_4, was added to the above equivalent circuit to represent this path. The value of the capacitance C_4 was found to be consistent with the high-frequency-limiting bulk capacitance of the specimens.

Appendix A: Metallographic Analysis to Obtain the Average Grain Size, D, and the Effective Intergranular Contact Area A_2 (17)

A representative micrograph used to determine the average grain size, D, is as shown in Fig. 1a. A line of length l_i is drawn randomly over the micrograph and the number of intersections n_i with the grain boundaries are counted. The procedure is repeated N times and the average length D between two consecutive boundaries is defined as the average grain size, i.e.,

$$D = \frac{1}{N}\sum_{i=1}^{N}\frac{l_i}{n_i - 1}. \tag{A1}$$

The effective intergranular area, A_2, can be estimated by considering a square section of the micrograph with length L and two individual grains with "projected boundary" λ as shown in Fig. A1. In this representation λ is the line intersection of the plane of polish with the intergranular surface. Consider an arbitrarily drawn line A with length L along the x axis. The probability that line A will intersect an infinitesimal element $d\lambda$ can be easily shown as

$$P = \frac{dx}{L}, \qquad = \frac{\cos\theta}{L}\,d\lambda. \tag{A2}$$

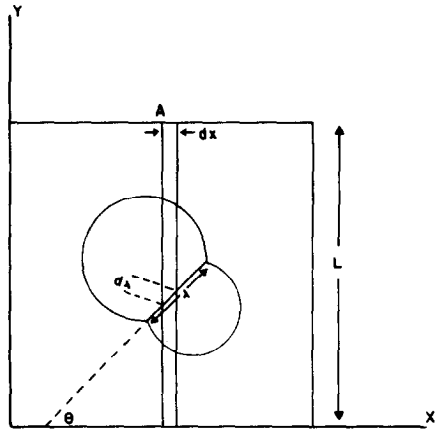

FIG. A1. Schematic representation of a small section of the micrograph.

Therefore, if N arbitrarily orientated lines are drawn, the average number of intersections formed per unit length of test line which will intersect the projected boundary λ is given by

$$\bar{N}_L = \int_0^{\lambda}\frac{1}{2\pi}\int_0^{2\pi}\frac{N((\cos\theta)/L)}{NL}\,d\lambda\,d\theta, \qquad = \frac{2}{\pi}\frac{\lambda}{L^2}. \tag{A3}$$

Here, NL is the total length of line constructed. From Eqs. (A1) and (A3), the total length of projected boundaries per unit area is

$$L_A = \lambda/L^2 = (\pi/2)/\bar{N}_L = (\pi/2)\cdot(1/D). \tag{A4}$$

Therefore, if, on the micrograph, the total number of projected boundaries, n', within an area, A, is counted, the average projected boundary length can be expressed as

$$\lambda \sim L_A(A/M^2). \tag{A5}$$

Here, M is the linear magnification factor of the microscope. The effective intergranular area can then be estimated as

$$A_2 = (\pi/4)\lambda^2. \tag{A6}$$

Appendix B: Equivalent Circuit Representations for an Idealized Sample Having a Cubical Packing of Spherical Grains

Consider that the specimen consists of uniform spherical grains and that all the grain boundaries are identical. Figure B1 represents a single boundary and its neighboring grains. Here, l_2 is the effective thickness of the boundary, A_2 is the effective intergranular contact area between two grains, and D is the average grain diameter. The resistance, R'_2, of such a single boundary would simply be

$$R'_2 = \rho_2(l_2/A_2), \tag{B1}$$

where ρ_2 is the effective resistivity of the boundary. The capacitance of this single boundary, C'_2, would be

$$C'_2 = \varepsilon_2\varepsilon_0(A_2/l_2), \tag{B2}$$

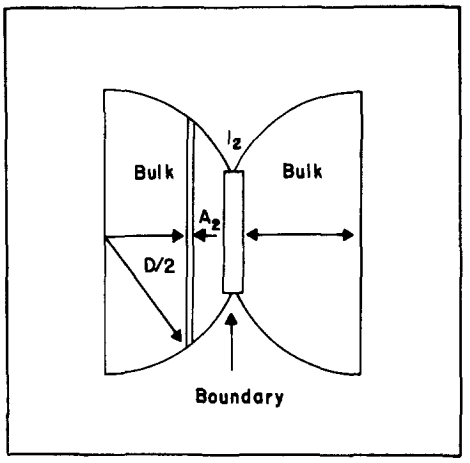

FIG. B1. Schematic representation of a boundary and its neighboring grains.

where ε_2 is the dielectric constant of the boundary and ε_0 is 8.854×10^{-14} F/cm.

An approximate expression for the resistance, R_1', of a single grain can be obtained by integrating the resistance associated with an infinitesimal section as shown in Fig. B1, i.e.,

$$R_1' = 2\rho_1 \int_0^{\gamma} \frac{dr}{\pi[(D/2)^2 - \gamma^2]}. \tag{B3}$$

Here, ρ_1 is the resistivity of the grain. Since

$$\pi[(D/2)^2 - \gamma'^2] \sim A_2, \tag{B4}$$

γ' can be expressed as

$$\gamma' = ((D/2)^2 - A_2/\pi)^{1/2}. \tag{B5}$$

From Eqs. (B3) and (B5) it can be shown that:

$$R_1' = \rho_1 \int_0^{[(D/2)^2 - A_2/\pi]^{1/2}} \frac{dr}{\pi[(D/2)^2 - \gamma^2]}$$

$$= \frac{2\rho_1}{\pi D} \log \frac{\pi^{1/2} D + (\pi D^2 - 4A_2)^{1/2}}{\pi^{1/2} D - (\pi D^2 - 4A_2)^{1/2}}. \tag{B6}$$

Similarly, it can be shown that

$$C_1' = \frac{\pi D \varepsilon_1 \varepsilon_0}{2} \left[\log \frac{\pi^{1/2} D + (\pi D^2 - 4A_2)^{1/2}}{\pi^{1/2} D - (\pi D^2 - 4A_2)^{1/2}} \right]^{-1}. \tag{B7}$$

where, ε_1 is the dielectric constant of the bulk grain. The total boundary resistance, R_2, can be estimated by considering that the specimen consists of the resistors, R_2', connected in series in the direction of the electric field and in parallel in the direction perpendicular to the electric field. If the specimen has thickness L and electrode area A, the number of R_2' in series would be

$$N_1 \sim L/D, \tag{B8}$$

while the number of R_2' in parallel would be

$$N_2 \sim (1/\alpha) \cdot (A/D^2). \tag{B9}$$

Here, α is a geometric factor related to the packing of the grains within a sample (for a simple cubic array of spherical grains, $\alpha \sim \pi/4$). From Eqs. (B1), (B8), and (B9) it can be shown that

$$R_2 \sim \rho_2 \frac{l_2}{A_2} \cdot \frac{L}{D} \cdot \frac{1}{(1/\alpha) \cdot (A/D^2)}$$

$$= \rho_2 \left[\frac{l_2}{A_2}\right] \alpha \left[\frac{L}{A}\right] D$$

$$= R_2' \alpha \left[\frac{L}{A}\right] D. \tag{B10}$$

Similarly, the total-boundary capacitance, C_2, the total bulk resistance, R_1, and the total bulk capacitance, C_1, can be expressed, respectively, as

$$C_2 = \varepsilon_2 \varepsilon_0 \left[\frac{A_2}{l_2}\right] \frac{1}{\alpha} \left[\frac{A}{L}\right] \frac{1}{D}$$

$$= C_2' \frac{1}{\alpha} \left[\frac{A}{L}\right] \frac{1}{D}, \tag{B11}$$

$$R_1 = R_1' \alpha \left[\frac{L}{A}\right] D, \tag{B12}$$

and

$$C_1 = C_1' \frac{1}{\alpha} \left[\frac{A}{L}\right] \frac{1}{D}. \tag{B13}$$

In a previous study (*38*) another simple approximation was used to express R_1, i.e.,

$$R_1 = \rho_1 (L/A) \cdot (1/\rho_{th}) \tag{B14}$$

Here, ρ_{th} is the percentage theoretical density of the sample. In this study Eq. (B14) was only used to estimate the bulk resistivity ρ_1. On other occasions, Eq. (B12) was considered.

A relaxation time, τ_2, which eliminates the geometric parameters can be defined as

$$\begin{aligned}\tau_2 &= R_2C_2 \\ &= R_2'C_2' \\ &= \rho_2\varepsilon_2\varepsilon_0.\end{aligned} \tag{B15}$$

References

1. T. H. Etsell and S. N. Flengas, *Chem. Rev.* **70**, 339 (1970).
2. P. Duwez, F. Odell, and F. H. Brown, Jr., *J. Amer. Ceram. Soc.* **35**, 107 (1952).
3. T. Y. Tien and E. C. Subbaroo, *J. Amer. Ceram. Soc.* **39**, 1041 (1963).
4. W. D. Kingery, J. Pappis, M. E. Doty, and D. C. Hill, *J. Amer. Ceram. Soc.* **42**, 393 (1959).
5. J. W. Patterson, E. C. Bogren, and R. A. Rapp, *J. Electrochem. Soc.* **114**, 752 (1967).
6. J. M. Dixon, L. D. LaGrange, J. Merten, C. F. Miller, and J. T. Parter, II, *J. Electrochem. Soc.* **110**, 276 (1963).
7. T. Y. Tien, *J. Amer. Ceram. Soc.* **47**, 430 (1964).
8. F. A. Kröger, *J. Amer. Ceram. Soc.* **49**, 215 (1966).
9. H. A. Johansen and J. G. Cleary, *J. Electrochem. Soc.* **111**, 100 (1964).
10. R. E. Carter and W. L. Roth, *in* "EMF Measurements in High-Temperature Systems" (C. B. Alcock, Ed.), p. 125, Inst. Min. and Met., London (1968).
11. F. Hund, *Z. Phys. Chem.* **199**, 142 (1952).
12. H. Yanagida, R. J. Brook, and F. A. Kröger, *J. Electrochem. Soc.* **117**, 593 (1970).
13. R. J. Brook, W. L. Pelzmann, and F. A. Kröger, *J. Electrochem. Soc.* **118**, 185 (1971).
14. T. Y. Tien, *J. Appl. Phys.* **35**, 122 (1964).
15. J. E. Bauerle, *J. Phys. Chem. Solids* **30**, 2657 (1969).
16. S. Chu, Ph.D. Dissertation, Marquette University, Milwaukee, Wisc. (1976).
17. R. T. DeHoff and F. N. Rhines, in "Quantitative Microscopy," McGraw–Hill, New York (1968).
18. M. A. Seitz, R. T. McSweeney, and W. M. Hirthe, *Rev. Sci. Instrum.* **46**, 826 (1969).
19. E. E. Hahn, *J. Appl. Phys.* **22**, 888 (1951).
20. A. D. Franklin, S. Marzallo and J. B. Wachtman, Jr., *J. Res. Nat. Bur. Stand. Sect.* **11A**, 355 (1967).
21. J. Volger, *Physica* **20**, 49 (1954).
22. R. W. Powers and S. P. Mitoff, *J. Electrochem. Soc.* **122**, 226 (1975).
23. K. Lehovoc, *J. Chem. Phys.* **21**, 1123 (1953).
24. A. R. Allnatt, *J. Phys. Chem.* **68**, 1763 (1964).
25. K. L. Kliewer and J. S. Koehler, *Phys. Rev.* **140**, A1226 (1965).
26. K. L. Kliewer, *Phys. Rev.* **140**, A1241 (1965).
27. W. D. Kingery, *J. Amer. Ceram. Soc.* **57**, 1 (1974).
28. W. D. Kingery, *J. Amer. Ceram. Soc.* **57**, 74 (1974).
29. K. W. Lay, Ph.D. Dissertation, Northwestern University, Evanston, Ill. (1966).
30. J. R. Macdonald, *J. Chem. Phys.* **61**, 3977 (1974).
31. M. A. Seitz and T. O. Sokoly, *J. Electrochem. Soc.* **121**, 163 (1974).
32. M. A. Seitz and T. B. Holliday, *J. Electrochem. Soc.* **121**, 122 (1974).
33. M. A. Seitz, R. T. McSweeney, and W. M. Hirthe, *J. Electrochem. Soc.* **120**, 259 (1973).
34. J. H. Beaumont and P. W. M. Jacobs, *J. Phys. Chem. Solids* **28**, 657 (1967).
35. R. J. Friauf, *J. Chem. Phys.* **22**, 1329 (1954).
36. R. T. McSweeney, Ph.D. Dissertation, Marquette University, Milwaukee, Wisc. (1974).
37. K. J. Vetter, *in* "Electrochemical Kinetics," p. 200, Academic Press, New York (1967).
38. F. S. Brugner, Ph.D. Dissertation, Marquette University, Milwaukee, Wisc. (1971).